

Frequency-domain cascading microwave superconducting quantum interference device multiplexers; beyond limitations originating from room-temperature electronics

Satoshi Kohjiro  and Fuminori Hirayama

National Institute of Advanced Industrial Science and Technology, 1-1-1 Umezono, Tsukuba, Ibaraki, 305-8568, Japan

E-mail: s-kohjiro@aist.go.jp

Received 20 August 2017, revised 13 December 2017

Accepted for publication 22 December 2017

Published 1 February 2018



CrossMark

Abstract

A novel approach, frequency-domain cascading microwave multiplexers (MW-Mux), has been proposed and its basic operation has been demonstrated to increase the number of pixels multiplexed in a readout line U of MW-Mux for superconducting detector arrays. This method is an alternative to the challenging development of wideband, large power, and spurious-free room-temperature (300 K) electronics. The readout system for U pixels consists of four main parts: (1) multiplexer chips connected in series those contain U superconducting resonators in total. (2) A cryogenic high-electron-mobility transistor amplifier (HEMT). (3) A 300 K microwave frequency comb generator based on $N(\equiv U/M)$ parallel units of digital-to-analog converters (DAC). (4) N parallel units of 300 K analog-to-digital converters (ADC). Here, M is the number of tones each DAC produces and each ADC handles. The output signal of U detectors multiplexed at the cryogenic stage is transmitted through a cable to the room temperature and divided into N processors where each handles M pixels. Due to the reduction factor of $1/N$, U is not anymore dominated by the 300 K electronics but can be increased up to the potential value determined by either the bandwidth or the spurious-free power of the HEMT. Based on experimental results on the prototype system with $N = 2$ and $M = 3$, neither excess inter-pixel crosstalk nor excess noise has been observed in comparison with conventional MW-Mux. This indicates that the frequency-domain cascading MW-Mux provides the full (100%) usage of the HEMT band by assigning N 300 K bands on the frequency axis without inter-band gaps.

Keywords: microwave SQUID multiplexer, RF-SQUID, transition edge sensor (TES), frequency-domain multiplexing, metallic magnetic calorimeter (MMC)

(Some figures may appear in colour only in the online journal)

1. Introduction

Microwave superconducting quantum interference device (SQUID) multiplexers (MW-Mux) [1, 2] are attracting much attention for readout circuits of superconducting detector array such as transition edge sensors (TES) [3] and metallic

magnetic calorimeters [4], and superconducting quantum bits for the quantum annealing [5]. The advantage of MW-Mux compared to conventional multiplexers [6] such as time-division, code-division, and frequency-division in MHz range is the larger bandwidth and the lower dissipation power at ≈ 0.1 K stage suitable for increasing the number of pixels

multiplexed in a readout cable U . Recently, MW-Mux for readout of 128-pixels gamma-ray TES was demonstrated [7] as a milestone of 512-pixels operation. Though the superconducting chip at the cryogenic stage is simple, sophisticated room-temperature (300 K) electronics [8–11] will be necessary for large U in future MW-Mux. In the 300 K electronics, there exist three restrictions for determining U .

The first restriction is the bandwidth [7]. The number of pixels multiplexed in a readout line is given by

$$U = \frac{B}{kf_s} \quad (1)$$

with

$$\kappa \equiv \frac{\Delta f_R}{f_s}, \quad (2)$$

where B is the readout frequency band ideally determined by the bandwidth of the cryogenic isolator followed by the cryogenic high-electron-mobility transistor amplifier (HEMT), f_s the readout bandwidth per pixel, Δf_R the difference of two neighboring resonance frequencies f_R . The inter-pixel crosstalk ≤ -30 dB requires $k \geq 10$ [2]. From typical values of parameters such as $B \approx 4$ GHz, $f_s \approx 0.1$ MHz, and $k \approx 10$, $U \approx 4 \times 10^3$ is predicted. In contrast, applicable for spectrometers with the resolving power $\geq 10^3$, the typical bandwidth of analog-to-digital converters (ADC) commercially available is less than 1 GHz [7]. Thus, the practical readout bandwidth B cannot reach the potential bandwidth of cryogenic circuits.

The second restriction is the noise of ADC that increases with the number of tones M processed in an ADC. Bennett *et al* showed theoretical analysis that the optimum signal-to-noise ratio due to ADC depends on M on the basis of the trade-off between quantization noise and clipping noise [10]. Rantwijk *et al* verified experimentally that the amplitude noise of microwave readout of microwave kinetic inductance detectors (MKID) increases with M for $M > 100$ and the ADC noise is larger than the HEMT noise for $M > 700$ when each tone power at MKID is $P_T \approx -91$ dBm [11]. Since the contribution of the HEMT noise is inversely proportional to P_T [12], the ratio of ADC noise to the HEMT noise should be discussed by taking into account of much larger value of $P_T \approx -76$ dBm to minimize the SQUID noise in our MW-Mux [13]. This suggests that ADC for MW-Mux may handle smaller M than ADC for MKID.

The third restriction not reported previously is the maximum power under which all microwave components in the readout circuit operates properly, e.g., with linear response and negligible spurious. If this is enough large, this restriction is determined by the ratio of saturation power of the HEMT to the optimum power of a tone $P_T \approx -76$ dBm [13] of our MW-Mux, that is similar to $P_T \approx -72$ dBm [7] and -70 dBm [4] reported by other groups. For a HEMT produced by California Institute of Technology [14], we got the experimental 1 dB compression $P_{H-Sat} \approx -36$ dBm at the input, that is similar to $P_{H-Sat} \approx -40$ dBm reported for another HEMT for readout of MKID [11]. From these, $P_{H-Sat}/P_T \approx 1 \times 10^4$ pixels can be in principle multiplexed

in our MW-Mux. However, for our conventional MW-Mux, not the HEMT but the 300 K electronics restricts $U < 100$ in terms of spurious-free power as described in section 2.

To overcome these limitations of U , in this paper, we have proposed frequency-domain cascading MW-Mux consisting of a cryogenic circuit and multiple 300 K electronics. In this system, the output signal of U detectors multiplexed at the cryogenic stage is transmitted through a cable to the room temperature and divided into N processors where each handles M pixels. We have found that appropriate low-pass filters (LPF) acting as anti-aliasing in both ADC and digital-to-analog converters (DAC) can eliminate guard bands supposed to be required for preventing the crosstalk among the cascaded N signal bands.

2. System description

2.1. Construction

Figure 1(a) shows the block diagram of frequency-domain cascading MW-Mux. The system consists of one cryogenic circuit and N 300 K signal-processing modules. The latter are connected to each other like a family-tree and the combined output of N DAC and combined input of N ADC in 300 K modules are connected to the former in series. At the cryogenic stage, several MW-Mux chips which consist of U superconducting microwave resonators in total are connected in series through each microwave feedline followed by a conventional cryogenic isolator and a HEMT. The function of DAC and ADC in each 300 K module is the same as that of conventional MW-Mux. The 300 K modules also contains N pairs of up-converters and down-converters those are pumped by N local oscillators (LO) with unique LO frequencies of f_{C1} , f_{C2} , ..., and f_{CN} phase-locked to a common crystal oscillator. This frequency-conversion system first up-converts N intermediate-frequency (IF) bands to the cascaded microwave bands to match the band of the HEMT. Each IF band contains M microwave tones. At the chips on the cryogenic stage, as ordinary, these tones are amplitude- and phase-modulated by the output of corresponding detector simultaneously. Finally, in the 300 K electronics, the modulated tones are divided into N down-converters whose outputs form N IF bands shown in figure 1(b). Signals of M modulated tones in each IF band are digitized by own ADC, i.e., N ADC in parallel are capable of processing $U = N \times M$ tones a HEMT handles. The guard bands shown in figure 1(b), buffer zones without tones, were assumed as a way to suppress the interference among modules. The drawback of the guard bands is preventing the full usage of the HEMT band for maximizing U . We have found our filtering techniques described in section 2.3 can eliminate the guard bands. Other idle zones for the margin against run-to-run and chip-to-chip variations of f_R may be required. As a convenience, table 1 summarizes the classification of alphabets and numbers adopted in this paper. In conclusion, this construction can solve three limitations on U described in chapter 1.

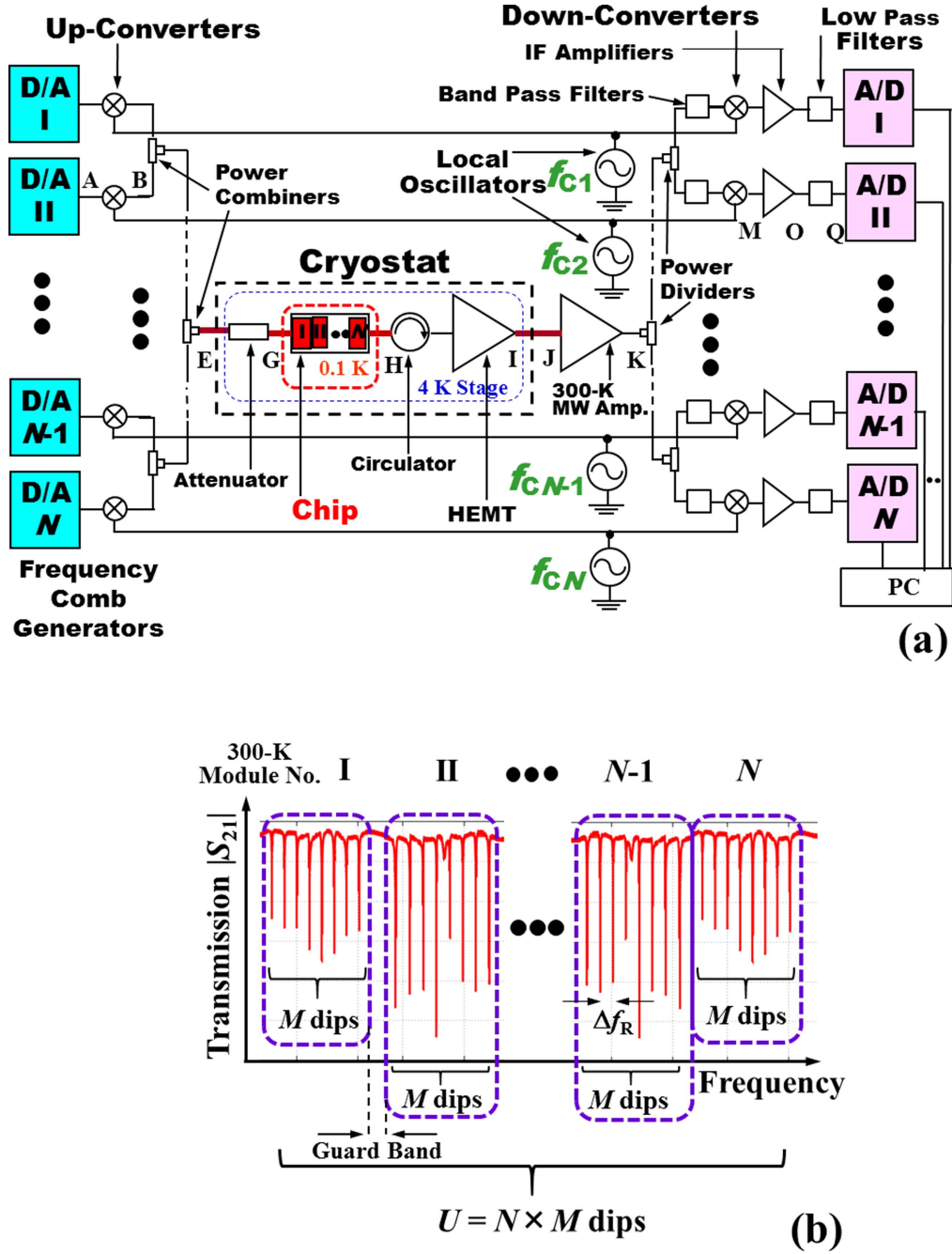


Figure 1. (a) Block diagram of a frequency-domain cascading MW-Mux. Node alphabets correspond to the horizontal axis in figure 3. Though IQ mixers are adopted for up-converters and down-converters as shown in figure 5(a), one mixer symbol denotes this IQ mixer in figure (a). (b) Frequency allocation of N IF bands provided by 300 K electronics in the operation of the frequency-domain cascading MW-Mux for U -pixel detectors. The guard bands, to suppress the interference among modules in compensation for preventing the full usage of frequency band, can be eliminated by our filtering techniques described in section 2.3.

Table 1. Category of alphabets and numerals adopted in this paper.

Character	Meaning	Figures	Table
A, B, ..., Q, R	Node of readout circuit	1(a), 2, 3	—
a, b, \dots, g, h	Tones produced in module I	6	—
i, j, \dots, o, p	Tones produced in module II	6	—
I, II, ..., $N-1, N$	300 K module	1, 5(a), 8, 9	—
1, 2, ..., 8, ..., M, \dots, U	Pixel	1(b), 8, 9	3

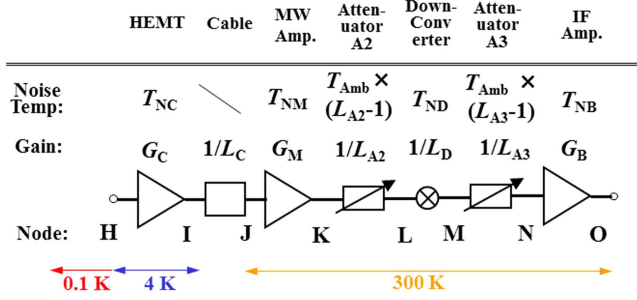


Figure 2. Components between HEMT and IF amplifiers in figure 1(a) and their noise temperatures at the input and power gains which contribute to determine η_N in equation (4). Nodes denoted by alphabet correspond to the horizontal axis in figure 3.

2.2. Beyond power-margin bottleneck

White noise of MW-Mux is dominated by the HEMT noise [7, 13]. Figure 2 shows the block diagram of selected components those contribute to the system noise. Two variable attenuators A2 and A3 omitted in figure 1 are adopted to adjust the power in the following down-converter and IF amplifier. The system noise temperature referred to the HEMT is given by

$$T_{NSH} = T_{NC}(1 + \eta_N) \quad (3)$$

with

$$\eta_N = \frac{L_C}{G_C} \left\{ \frac{T_{NM}}{T_{NC}} + \frac{1}{G_M} \frac{T_{Amb}(L_{A2} - 1)}{T_{NC}} + \frac{L_{A2}}{G_M} \times \left[\frac{T_{ND}}{T_{NC}} + \frac{T_{Amb}}{T_{NC}} L_D (L_{A3} - 1) + L_D L_{A3} \frac{T_{NB}}{T_{NC}} \right] \right\}, \quad (4)$$

where T_{NC} , T_{NM} , T_{ND} , T_{NB} are the noise temperature, G_C , G_M the power gain, L_C , L_D , L_{A2} , L_{A3} the loss of components shown in figure 2 and T_{Amb} the ambient temperature at which the attenuators operate. Once the criterion of η_N is proposed, e.g., $\eta_N \leq 0.3$ in this paper, several solutions of L_{A2} and L_{A3} are given so that equation (4) is satisfied. Though L_{A2} and L_{A3} contribute equally to the power margin for spurious free, equation (4) indicates L_{A2} and L_{A3} increase η_N in a different manner. The attenuation L_{A3} increases the noise contribution of only two components, i.e., the attenuator A3 and the IF amplifier, while L_{A2} increases that of four components, i.e., not only A3 and IF amplifier, but also A2 and the down-converter. Among several solutions of L_{A2} and L_{A3} , the optimum one should be chosen from the trade-off between lower η_N and larger power margin for spurious free as discussed in later.

Figure 3 shows the power level diagram of a pixel under the lowest noise in our MW-Mux. The dashed, dashed-dotted, and bold solid lines denote three cases to satisfy $\eta_N = 0.3$ with three pairs of L_{A2} and L_{A3} listed in table 2. As shown in figure 3, the IF amplifier determines the system power margin P_{MB} listed in table 2 for these three cases as a criterion of four power ratios of spurious to the fundamental $I^* = -30, -40, -50$, and -60 dB. These values are estimated from the

specification of output IP3 (the two-ton third-order intercept point).

Though P_{MB} increases with L_{A3} for $L_{A3} \leq 20$ dB in table 2, such trend saturates for $L_{A3} > 20$ dB, when the noise contributed from the attenuator A3 and/or the IF amplifier, i.e., $(L_{A2}/G_M)(T_{Amb}/T_{NC})L_D(L_{A3}-1)$ and/or $(L_{A2}/G_M)L_D L_{A3}(T_{NB}/T_{NC})$, respectively, becomes dominant in the right-hand side of equation (4). In this region with approximations of $L_{A2} \gg 1$, $L_{A3} \gg 1$, $T_{ND} \approx T_{Amb}(L_D-1)$, and when the first term $(L_C/G_C)(T_{NM}/T_{NC})$ is negligibly small, equation (4) is approximated to

$$L_{A2}L_{A3} \approx \eta_N \frac{G_C G_M}{L_C L_D} \frac{T_{NC}}{T_{Amb} + T_{NB}}. \quad (5)$$

Equation (5) indicates that η_N determines the $L_{A2}L_{A3}$ product, i.e., the power margin at the IF amplifier output. Thus, for $L_{A3} > 20$ dB and $0 \ll L_{A2} < 28.5$ dB, any combination of L_{A2} and L_{A3} that satisfies equation (5) provides the same power margin at the IF amplifier as that of (c) in figure 3.

From P_{MB} for (c) in figure 3, the maximum number of pixels multiplexed in a 300 K module M is calculated as $M = 80$ for the criterion of $I^* = 30$ dB, $M = 25$ for $I^* = 40$ dB, $M = 8$ for $I^* = 50$ dB, and $M = 2$ for $I^* = 60$ dB. These values are two or three orders of magnitude smaller than the intrinsic value determined by P_{H-Sat}/P_T described in section 1. Thus, in the conventional MW-Mux, a 300 K module is the bottleneck for increasing M not only on frequency band but also on spurious-free power. Frequency-domain cascading MW-Mux joins signals of all pixels distributed in N 300 K modules together into a coaxial cable between the cryogenic stage and 300 K, resulting in increasing both frequency band and spurious-free power N times as large as those of conventional MW-Mux. In the following sections, based on the prototype with $N = 2$, we show experimentally the spurious intensity as a function of number of tones and the effect of proper LPF on eliminating the guard band.

2.3. Band separation and anti-aliasing toward full usage of HEMT band

In frequency-domain cascading MW-Mux, the crosstalk between pixels belonging to another 300 K modules will increase due to the aliasing in DAC and ADC, and the harmonic mixing of up- and down-converters. To prevent the crosstalk among different modules, two kinds of filtering are important. The first filtering is bandpass filters (BPF) positioned at the input of the down-converter. Without these BPF, the output power of the 300 K microwave amplifier is divided into N down-converters. In other words, the input of each down-converter sees all tones of frequency combs produced in N DAC. When U , i.e., the total input power, is large, the ratio of the spurious to the fundamental component becomes large. Figure 4(e) shows the peak power of spurious versus number of input tones of microwave comb entering a mixer operating as an up-converter. Except for the intended tones of the frequency comb, spurious lines are seen in figures 4(a)–(d) whose description is in the caption. As shown, both the spurious intensity and the number of

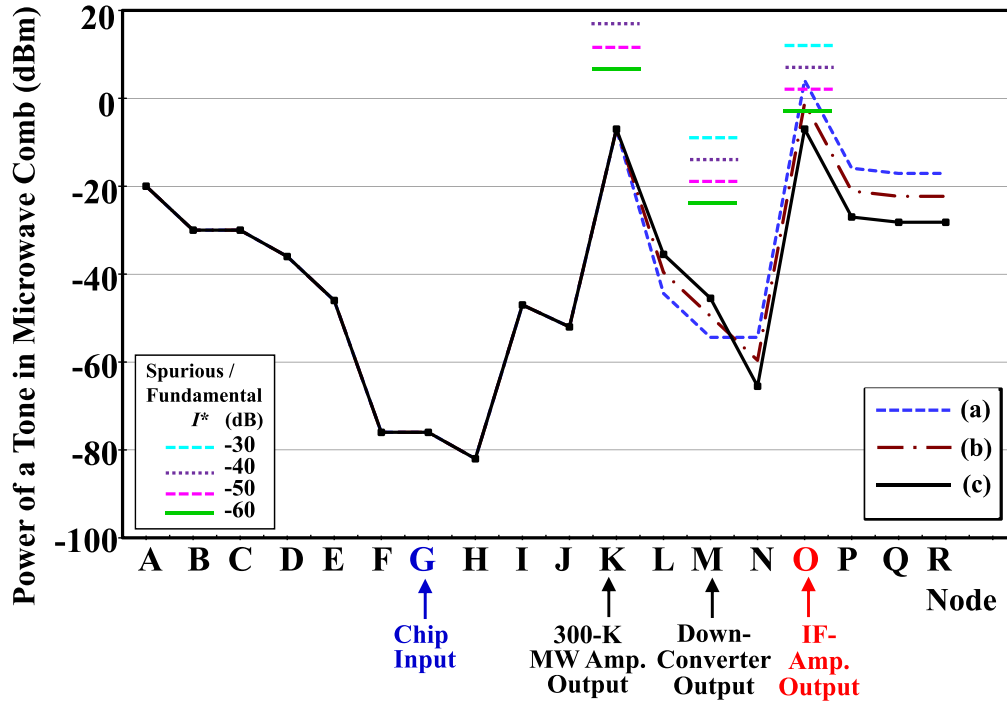


Figure 3. Power level diagrams of 1-pixel MW-Mux in AIST under the optimum power at the chip input $P_T = -76$ dBm. Alphabets at the horizontal axis denote node points; C, F, P, and R are not shown but others are marked in figures 1(a) or 2. Dashed, dashed-dotted, and solid lines satisfy $\eta_N = 0.3$ in equation (4), and denote the attenuations of variable attenuators as (a) $L_{A2} = 37.4$ dB and $L_{A3} = 0$ dB, (b) $L_{A2} = 32.6$ dB and $L_{A3} = 10$ dB, and (c) $L_{A2} = 28.5$ dB and $L_{A3} = 20$ dB, respectively. Other parameters in equation (4) are set as $T_{NC} = 3$ K, $T_{NM} = 170$ K, $T_{ND} \approx T_{Amb}(L_D - 1) = 2700$ K, $T_{NB} = 110$ K, $G_C = 35$ dB, $G_M = 45$ dB, $L_C = 5$ dB, and $L_D = 10$ dB. Blue dashed, purple dotted, pink dashed, and green solid bars at nodes K, M, and O denote the criteria of power-ratio of spurious to the fundamental as $I^* = -30$, -40 , -50 , and -60 dB, respectively; those are calculated from the specification of output IP3 (the two-ton third-order intercept point) of 300 K microwave amplifier (37 dBm at the node K), down-converter (6 dBm at M), and IF amplifier (27 dBm at O) adopted in our system.

Table 2. Loss of attenuators A2 and A3, and resulting power margin at the output port of the IF amplifier for 3 cases in figure 3.

Case	L_{A2} (dB)	L_{A3} (dB)	P_{MB} ($I^* = -30$ dB) (dB)	P_{MB} ($I^* = -40$ dB) (dB)	P_{MB} ($I^* = -50$ dB) (dB)	P_{MB} ($I^* = -60$ dB) (dB)
(a)	37.4	0	8	3	—	—
(b)	32.6	10	13	8	3	—
(c)	28.5	20	19	14	9	4

spurious lines increase rapidly with the increase of the number of tones. This spurious may prevent the proper operation of MW-Mux and degrade its performance. The BPF whose passband is slightly wider than band of the corresponding 300 K module limits the number of tones and power which enter each down-converter and expected to prevent the above-mentioned spurious. In our experiment on $N = 2$, BPF was not adopted because the excess tones and power entering into the mixer in other modules is serious problem only when N is large.

The next filtering is LPF positioned at the output of DAC and the input of the ADC. In the ADC case, the LPF decreases the intensity of the aliasing originating from frequency-comb tones in the neighboring channel. Figure 5(a) shows the experimental setup with $N = 2$ to demonstrate the effect of anti-aliasing of the LPF shown in figure 5(b). Figure 6 shows the experimental results of band separation between 300 K modules I and II. In each module, eight tones

of frequency comb are existing, i.e., tones a, b, \dots, g , and h in module I denoted by blue arrows and tones i, j, \dots, o , and p in module II by pink arrows. Figure 6(b) shows the spectrum of the down-converted and sampled signal corresponding to module I without the LPF. In addition to eight tones a, b, \dots, h originating from module I, tones i and j corresponding to module II are also shown in the proper frequency positions, since they are also in the band of $0 \leq f \leq f_{SA}/2$ where f_{SA} is the sampling frequency of the ADC. The information of detector output that modulates these ten tones are read properly out. In contrast, other six tones labeled as k, l, \dots, o , and p denoted by pink arrows become ‘aliasing.’ Since four aliasing tones labeled as m, n, o , and p are close to the original ones a, b, c , and d , respectively, these can cause the inter-channel crosstalk and degrade the readout performance. The origin of sub tones whose intensity $< 1 \times 10^{-2}$ in figure 6(b) is now under study except for the sideband noise due to the imperfection of the IQ mixers. Figure 6(c) shows the

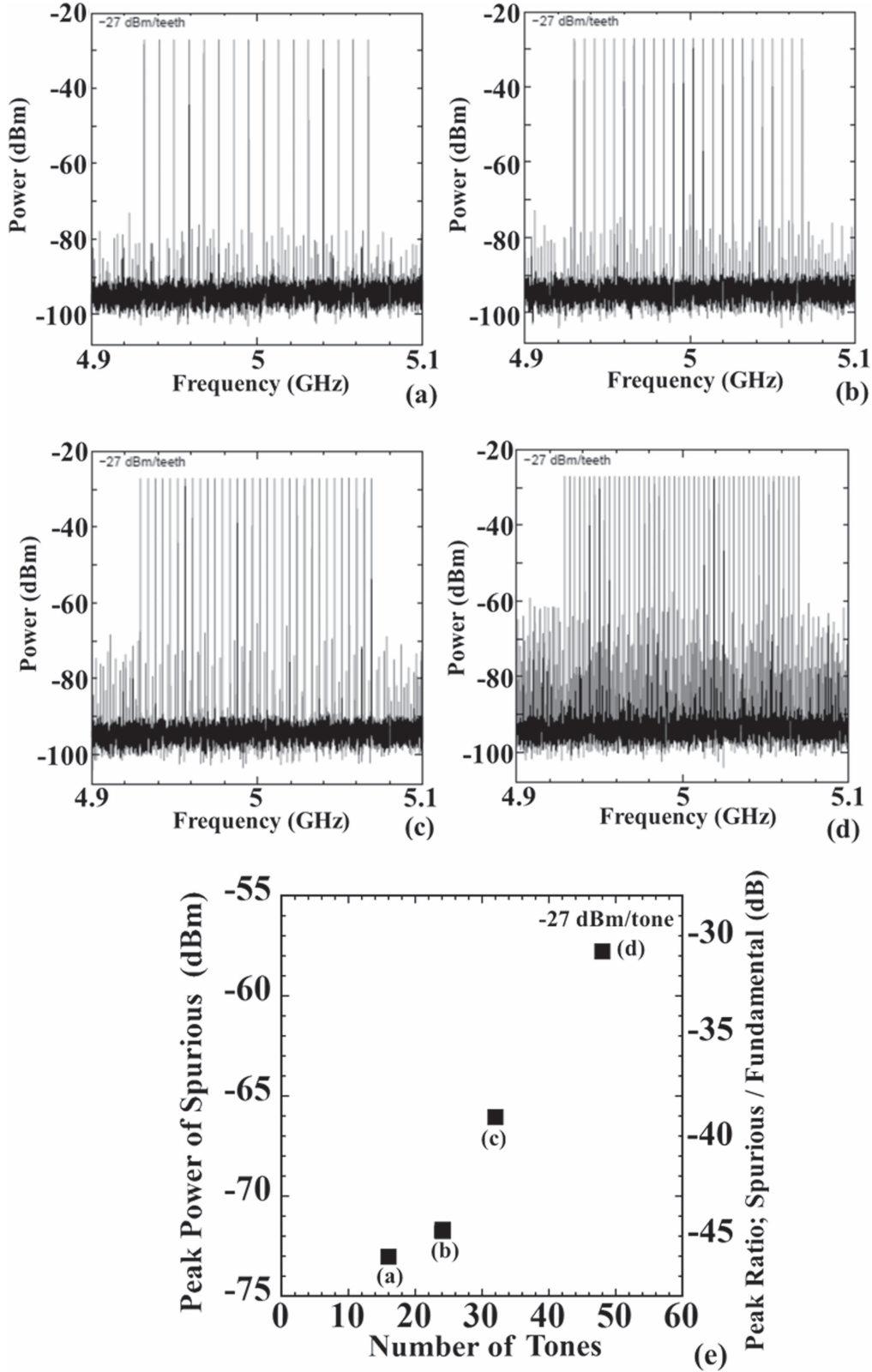


Figure 4. Spectrums of mixer output with the input number of tones of (a) 16, (b) 24, (c) 32, and (d) 48. (e) Output peak power of spurious (left) and its ratio to the power of input tone (right) versus number of tones entering a mixer operating as an *IQ* up-converter. Same mixer is adopted for an *IQ* down-converter. Input power is -27 dBm/tone.

down-converted signal corresponding to the module I with the LPF. The intensity of six aliasing tones decreases to be less than 1×10^{-5} of that of the original ones. This is

attributed to the attenuation of LPF for $f > f_c$ where f_c is the cutoff frequency of LPF. The intensity of the alias A_c (dB) at $f_{stop} = f_{SA} - f_c$ is determined by the specification of the LPF.

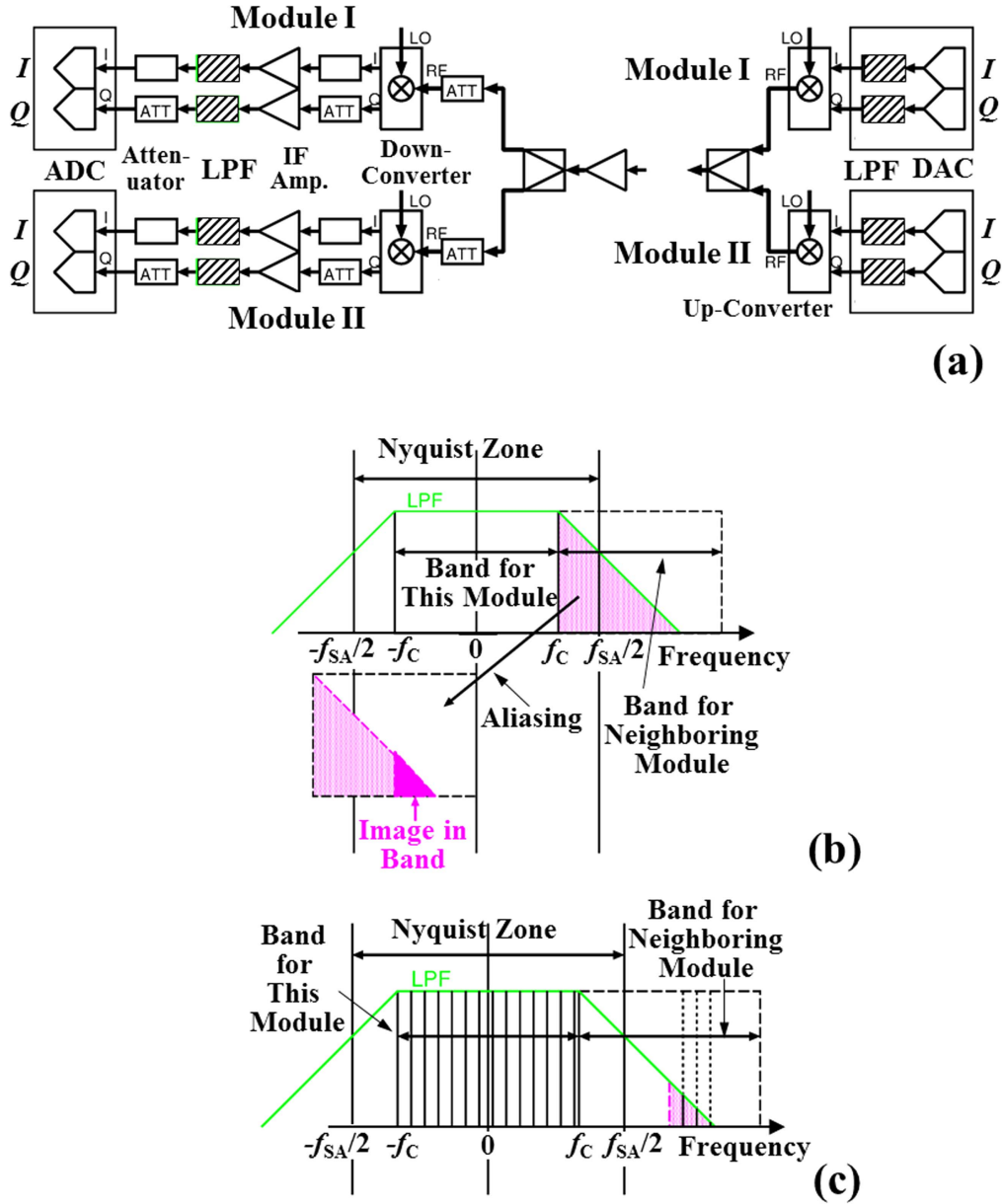


Figure 5. (a) Experimental setup with $N = 2$ for demonstration of band separation based on LPF denoted by hatched rectangles. Concept of band separation due to the anti-aliasing assisted by the low-pass filter for ADC (b) and DAC (c), where green lines indicate the transmission versus frequency of LPF.

Though the available frequency band of ADC can be fully used for $f_{SA}/(2f_C) \approx 1$, the guard band shown in figure 1(b) should be set to avoid the interference between modules I and II. In contrast, at the expense of the ADC band, choosing f_C that is not close to $f_{SA}/2$ as illustrated in figure 5(b) can avoid such guard band due to large f_{Stop} and A_C , resulting in the full use of the HEMT band by our frequency-domain cascading MW-Mux in the ideal case without deviation of f_R due to fabrication yield. In our experiment, 5-section discrete LPF with $A_C \geq 60$ dB at $f_{Stop} = 150$ MHz, $f_C = 90$ MHz, and $f_{SA} = 240$ MHz [15] exhibits the successful anti-aliasing. Same discussion is applicable to the aliasing comb which appears at the outside of the first Nyquist zone generated by the DAC shown in figure 5(c). Our LPF succeeded in

suppression of aliasing less than 1×10^{-5} without guard bands. This indicates that the frequency-domain cascading MW-Mux is capable of 100% usage of frequency resources provided by the HEMT without any guard bands shown in figure 1(b).

2.4. Common flux-ramp modulation for multiple 300 K modules

To linearize the response of SQUID corresponding to TES current, the flux-ramp modulation (FRM) methods was proposed [16]. We implemented the FRM in field-programmable gate array (FPGA)-based equipment as follows: the FPGA resets the ramp circuit periodically and thus the resulting sawtooth wave is completely synchronized with the FPGA

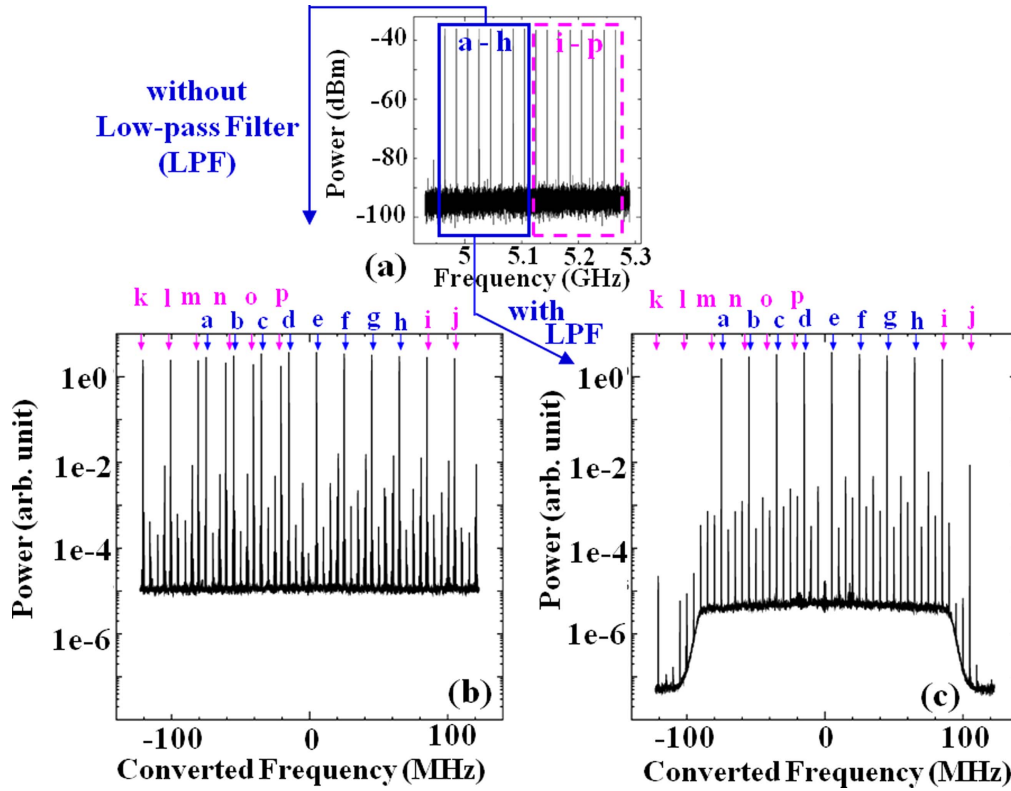


Figure 6. Experimental verification of anti-aliasing assisted by the low-pass filter shown in figure 5(a). (a) Power spectrum of *IQ* up-converter output. Tones in blue solid and pink dashed rectangles are generated in 300 K modules I and II, respectively. (b), (c) Power spectrum at the input of ADC in module I without (b) or with (c) low-pass filters. The origin of sub tones whose intensity $< 1 \times 10^{-2}$ in figure 6(b) is now under study except for the sideband noise due to the imperfection of the *IQ* mixers.

clock. This means that any SQUIDs controlled by one FPGA can share a common wire for the modulation. It is preferable that a common modulation wire can be shared across multiple FPGA-based modules for decreasing thermal flow into the cryogenic environment.

To demonstrate this concept by the prototype of $N = 2$, FPGA clocks on the two modules were synchronized with an external clock by phase-locked loop (PLL) hardware and the transient of sawtooth waves were aligned by the FPGA firmware functionality. We confirmed experimentally that the period and the phase of reset pulses for the FRM circuit on both modules were not deviated for a few days once they are synchronized. Thus, the flux-ramp modulation wave from one 300 K module can be employed by the other as if the modulation wave were from its own ramp circuit.

3. Feasibility demonstration based on prototype with $N = 2$

3.1. Inter-pixel crosstalk under no flux-ramp modulation (FRM)

Crosstalk under no FRM is evaluated by the shift of complex transmission coefficient $S_{21} = \text{Re}(S_{21}) + j\text{Im}(S_{21})$ of the scattering matrix of a MW-Mux chip shown in figure 7(a) from the initial value without crosstalk where $j^2 = -1$. Trajectories of S_{21} at $f \approx f_R$ traces a circle in the $\text{Re}(S_{21})$ - $\text{Im}(S_{21})$ plane and the

center angle θ varies with current applied to the input coil of the SQUID as shown in figure 7(b). For SQUIDs 2 and 7, i.e., the SQUIDs which terminate resonators in pixels 2 and 7, respectively, θ can be measured as θ_2 and θ_7 simultaneously. The difference of resonance frequency between pixels 2 and 7 is designed as 20 MHz that is equal or smaller than that of any other pixel pairs. Figure 7(c) shows θ_2 and θ_7 as a function of the input current of SQUID 7 I_7 for several input current to SQUID 2 I_2 obtained by conventional way. Without any crosstalk between 2 and 7, θ_2 is independent of I_7 . However, θ_2 slightly depends on I_7 and shows correlation with θ_7 , which is attributed to the crosstalk between pixels 2 and 7. The correlation becomes approximately a linear function of θ_7 as figure 7(d). Thus, the gradient $d\theta_2/d\theta_7$ exhibits the crosstalk strength. Figure 7(e) shows the dependence of $d\theta_2/d\theta_7$ on θ_2 when pixels 2 and 7 operate in a conventional or frequency-domain cascading regimes. We chose $\max.[d\theta_2/d\theta_7]$, the maximum crosstalk strength $d\theta_2/d\theta_7$ over the whole θ_2 range, as the figure of merit for evaluating crosstalk [17]. Figure 7(e) indicates $\max.[d\theta_2/d\theta_7] = 4.5 \times 10^{-3}$ in conventional and $\max.[d\theta_2/d\theta_7] = 4.1 \times 10^{-3}$ in the frequency-domain cascading regimes, respectively. Their difference in $\max.[d\theta_2/d\theta_7] = (4.5 - 4.1) \times 10^{-3} = 0.4 \times 10^{-3}$ is attributed to the shift of θ_2 that may be due to the slight change of critical current of the Josephson junction in the SQUID. Thus, the crosstalk strength between pixels 2 and 7 in the frequency-domain cascading regime is not larger than that in the conventional one.

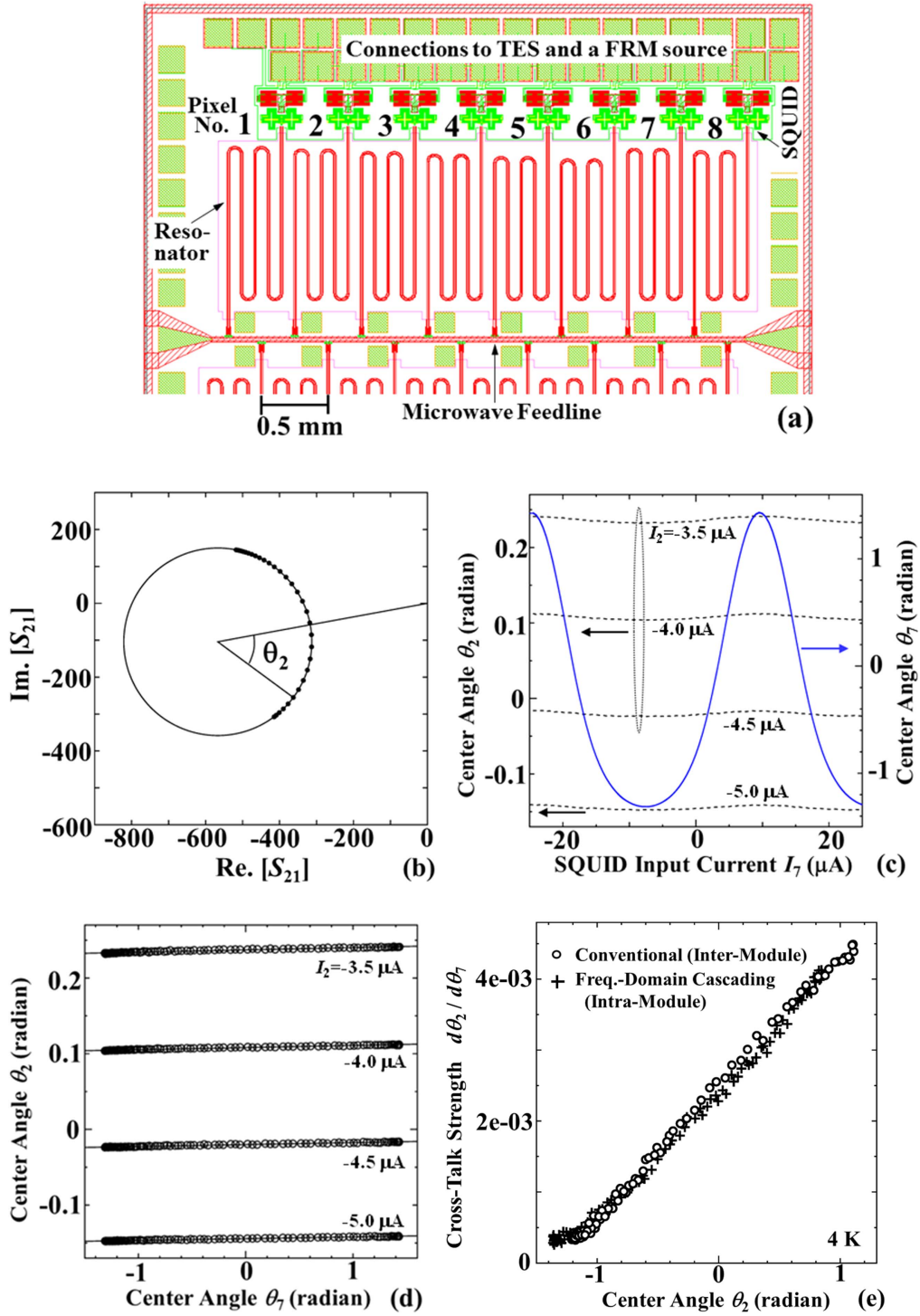


Figure 7. (a) Layout of the multiplexer. Eight resonators located on a side of a common feedline were used for the measurement. Difference of resonance frequency between the neighboring channels were 60 MHz except for the pair (6, 7) which had 260 MHz separation. (b) Resonance circle of SQUID 2. (c) Center angles of resonance circle of SQUIDs 2 (black dotted line) and 7 (blue solid line) versus input current of SQUID 7 for four values of input current of SQUID 2 I_2 . (d) Relation between center angle of SQUID 2 and that of 7 for four values of I_2 . Circles denote experimental results and solid lines linear fits. (e) Measured crosstalk strength from pixel 7 to 2 $d\theta_2/d\theta_7$ versus the center angle on resonance circle of 2 θ_2 where both pixels operate at 4 K with the same 300 K module in conventional regime (filled circles) or with the different 300 K modules in frequency-domain cascading regime (open circles) without the flux-ramp modulation.

3.2. Inter-pixel crosstalk under FRM

Crosstalk under FRM was characterized in both frequency-domain cascading and conventional regimes. In frequency-

domain cascading operation, common FRM described in section 2.4 was carried out. Figure 8 shows the flux referred to SQUID output of six pixels 1, 2, 3, 4, 5 and 6 (in order from top to bottom) shown in figure 7(a) versus input current

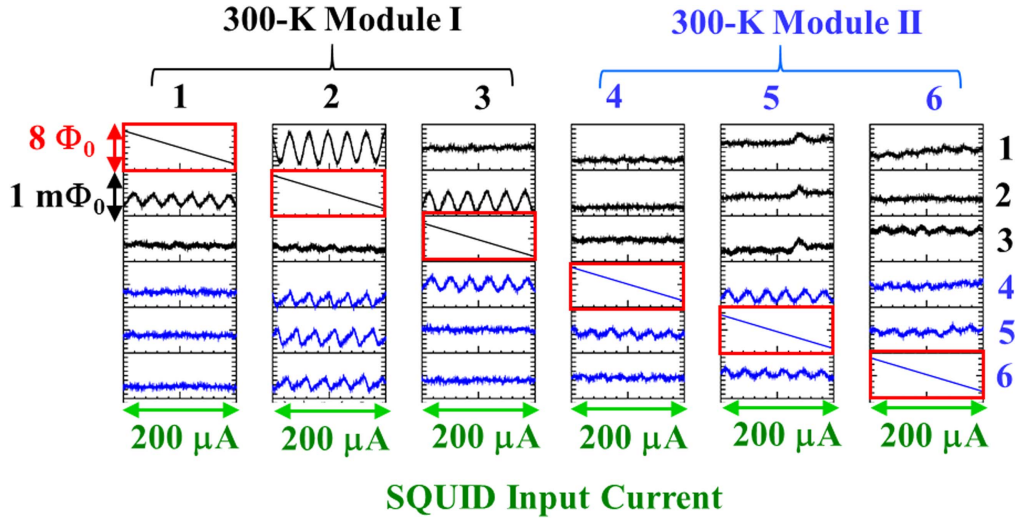


Figure 8. Demodulated output flux versus input current of the SQUID for six pixels in the frequency-domain cascading regime with FRM at 4 K, where pixels 1–3 cooperate with a 300 K module labeled as I, while the rest of the pixels 4–6 with another module II. Note that the full scale of the vertical axis is $8 \Phi_0$ for the diagonal panels but $1 \text{ m}\Phi_0$ for the off-diagonal ones.

Table 3. Measured crosstalk degree between neighboring pixels with $\Delta f_R = 60 \text{ MHz}$ under flux-ramp modulation (summary of figure 8).

Pair of pixel	3, 4	4, 3	1, 2	2, 1	2, 3	3, 2	4, 5	5, 4	5, 6	6, 5	Average
Freq.-Dom. Cascad.	1.5	2.8									2.2
Conventional			2.8	6.5	1.5	4.2	2.6	2.8	2.0	1.6	3.0

Numerical values are peak-to-peak output flux in the unit of $\times 10^{-4} \Phi_0$ shown in figure 8. Pair of pixel 3, 4 described at the left column in the top row denotes the crosstalk from pixel 3 to 4.

of the SQUID of pixels 1–6 (in order from left to right). In this experiment, three pixels 1–3 operate in a 300 K module, while the rest of the pixels 4–6 are in another module. Note that the full scale of vertical axis in diagonal panels is $8 \Phi_0$, while that of off-diagonal ones is $1 \text{ m}\Phi_0$, where $\Phi_0 \equiv h/(2e)$ is the flux quantum, h the Planck's constant, e the unit charge. The diagonal panels show linear input-output characteristics due to FRM. Some of off-diagonal panels exhibit response to the input flux with period of Φ_0 due to the crosstalk. The peak-to-valley value of output flux is less than $1 \text{ m}\Phi_{op-p}$ corresponding to the input flux change of Φ_0 , resulting in the corresponding crosstalk is order of 10^{-3} . To make clear the difference in the crosstalk between the conventional and frequency-domain cascading readout regimes, table 3 summarizes the crosstalk degree under FRM of all combinations of two pixels those are positioning in neighbor on the chip and $\Delta f_R = 60 \text{ MHz}$. This is an appropriate selection for their comparison since the crosstalk strength generally decreases and becomes difficult to be quantified due to the comparable noise with the increase of Δf_R or the separation of two pixels Δx [17]. There are four pairs those satisfy such condition in the conventional regime, i.e., (1, 2), (2, 3), (4, 5), and (5, 6), while the only one pair of (3, 4) in the frequency-domain cascading regime. The crosstalk degree of (3, 4) is $2.2 \times 10^{-4} \Phi_{op-p} < 3.0 \times 10^{-4} \Phi_{op-p}$, i.e., the average crosstalk degree among four pairs in a conventional system.

This indicates that excess crosstalk originating from the frequency-domain cascading operation is not found under FRM.

3.3. Noise under FRM

Figure 9 shows the measured frequency-dependent flux noise of pixels 1, 2, 3, 7 and 8 at 4 K in conventional ((a) and (c)) or frequency-domain cascading ((b) and (d)) regime. In frequency-domain cascading regime, pixels 1 and 7 operate with 300 K module I and the rest 2, 3 and 8 with module II. In both regimes, FRM is carried out and the white noise dominates above 30 Hz. Though about factor-2 deviation of noise is observed among these five pixels mainly due to the variation of unloaded quality factor of resonators Q_U , under the same input power of the down-converters, one can find the frequency-domain cascading MW-Mux exhibits the same white noise as the conventional one.

4. Conclusion

The advantage of frequency-domain cascading MW-Mux was quantitatively analyzed from the viewpoints of not only frequency band but also spurious-free power. The operation of a prototype with $N = 2$ and $U = 6$ was successfully demonstrated under FRM with a common modulation wire and exhibited neither excess crosstalk nor excess noise compared to the conventional MW-Mux. The proper anti-aliasing and filtering enable the

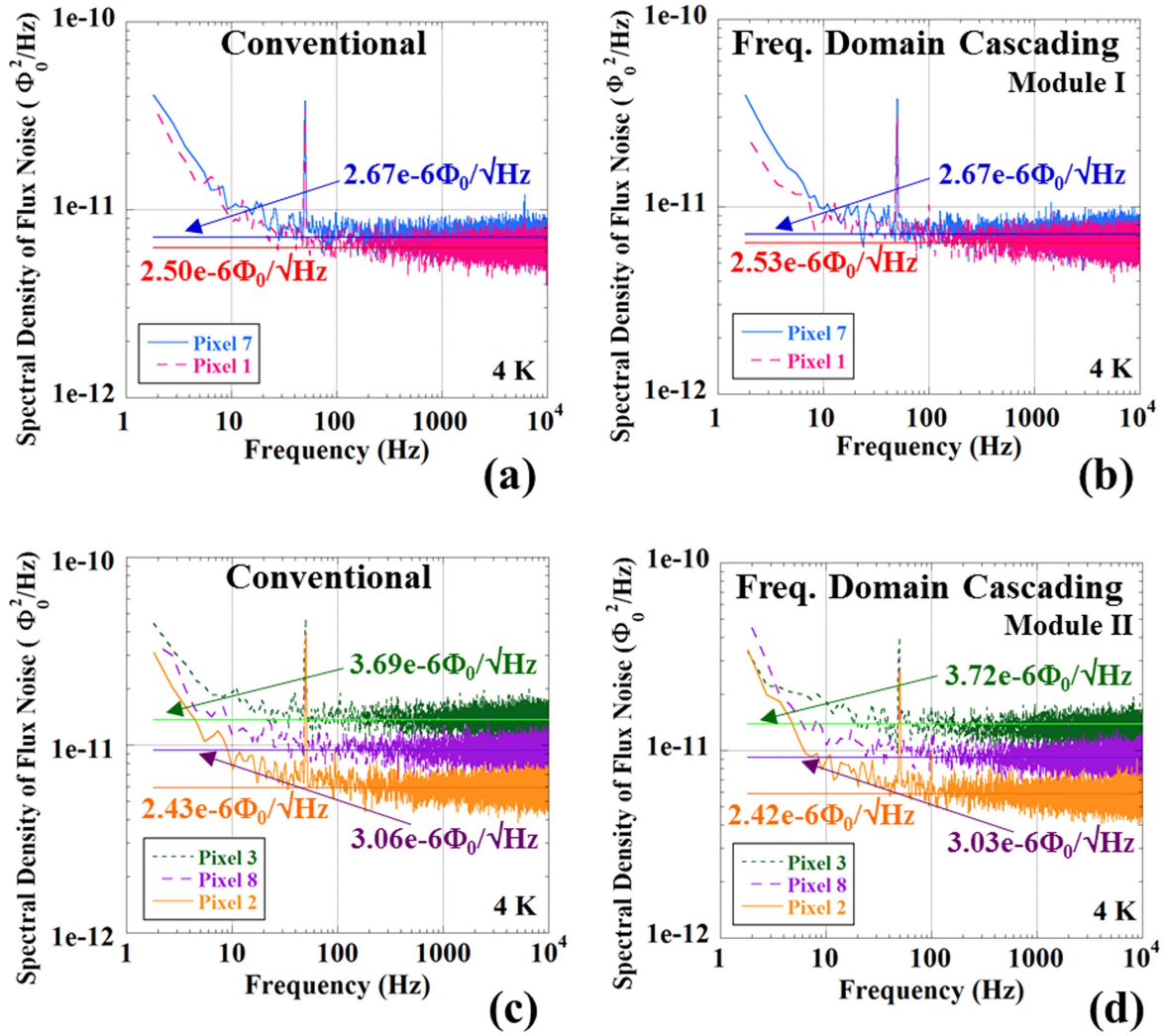


Figure 9. Spectral density of noise flux at SQUID versus frequency of pixels 1 and 7 at 4 K in the conventional (a) and frequency-domain cascading (b) regimes and those of pixels 2, 3 and 8 at 4 K in the conventional (c) and frequency-domain cascading (d) regimes. In the frequency-domain cascading regime, pixels 1 and 7 cooperate with 300 K module I, and 2, 3 and 8 do with module II. Horizontal solid lines denote white-noise levels those values are described.

frequency-domain cascading MW-Mux to be applicable for increasing U up to the potential value determined by the cryogenic HEMT amplifier, resulting in high-resolution spectrometers with large-format array detectors implemented in a small cryocooler with small power consumption.

Acknowledgments

The authors would like to acknowledge H Yamamori, S Nagasawa, and M Hidaka for fruitful discussion on the device fabrication, A Sato, D Fukuda, Y Sato, T Irimatsugawa, and Y Nakashima for discussion on the characterization of completed devices, and S Yamada in Tokyo Metropolitan University for the concept of room-temperature electronics. The MW-Mux chips were fabricated in the clean room for analog-digital superconductivity (CRAVITY) in National Institute of Advanced Industrial Science and Technology (AIST), Japan. This work was supported by JSPS KAKENHI Grant Number JP15H02251.

ORCID iDs

Satoshi Kohjiro <https://orcid.org/0000-0002-3001-1742>

References

- [1] Irwin K D and Lehnert K W 2004 Microwave SQUID multiplexer *Appl. Phys. Lett.* **85** 2107–9
- [2] Mates J A B, Hilton G C, Irwin K D, Vale L R and Lehnert K W 2008 Demonstration of a multiplexer of dissipationless superconducting quantum interference devices *Appl. Phys. Lett.* **92** 023514
- [3] Noroozian O *et al* 2013 High-resolution gamma-ray spectroscopy with a microwave-multiplexed transition-edge sensor array *Appl. Phys. Lett.* **103** 202602
- [4] Kempf S, Wegner M, Deeg L, Fleischmann A, Gastaldo L, Herrmann F, Richter D and Enss C 2017 Design, fabrication and characterization of a 64 pixel metallic magnetic calorimeter array with integrated, on-chip microwave SQUID multiplexer *Supercond. Sci. Technol.* **30** 065002

- [5] Whittaker J D *et al* 2016 A frequency and sensitivity tunable for high-speed quantum processor readout *J. Appl. Phys.* **119** 014506
- [6] Ullom J and Bennet D 2015 Review of superconducting transition-edge sensors for x-ray and gamma-ray spectroscopy *Supercond. Sci. Technol.* **28** 084003
- [7] Mates J A B *et al* 2017 Simultaneous readout of 128 x-ray and gamma-ray transition-edge microcalorimeters using microwave SQUID multiplexing *Appl. Phys. Lett.* **111** 062601
- [8] McHugh S, Mazin B A, Serfass B, Meeker S, O'Brien K, Duan R, Raffanti R and Werthimer D 2012 A readout for large arrays of microwave kinetic inductance detectors *Rev. Sci. Instrum.* **83** 044702
- [9] Madden T J *et al* 2017 Development of ROACH firmware for microwave multiplexed x-ray TES microcalorimeters *IEEE Trans. Appl. Supercond.* **27** 2500504
- [10] Bennett D A, Mates J A B, Gard J D, Hoover A S, Rabin M W, Reintsema C D, Schmidt D R, Vale L R and Ullom J N 2015 Integration of TES microcalorimeters with microwave SQUID multiplexed readout *IEEE Trans. Appl. Supercond.* **25** 2101405
- [11] van Rantwijk J, Grim M, van Loon D, Yates S, Baryshev A and Baselmans J 2016 Multiplexed readout for 1000-pixel arrays of microwave kinetic inductance detectors *IEEE Trans. Microwave Theory Tech.* **64** 1876–83
- [12] Zmuidzinas J 2012 Superconducting microresonators: physics and applications *Annu. Rev. Cond. Matter Phys.* **3** 169–214
- [13] Kohjiro S, Hirayama F, Yamamori H, Nagasawa S, Fukuda D and Hidaka M 2014 White noise of Nb-based microwave superconducting quantum interference device multiplexers with NbN coplanar resonators for readout of transition edge sensors *J. Appl. Phys.* **115** 223902
- [14] <http://cosmicmicrowavetechnology.com>
- [15] <http://lorch.com/home.html>
- [16] Mates J A B, Irwin K D, Vale L R, Hilton G C, Gao J and Lehnert K W 2012 Flux-ramp modulation for SQUID multiplexing *J. Low Temp. Phys.* **167** 707–12
- [17] Hirayama F *et al* 2017 Interchannel crosstalk and nonlinearity of microwave SQUID multiplexers *IEEE Appl. Supercond.* **27** 2500205